Articles   NanoLab

Preparation and Physical Properties of Functional Barium Carbonate Nanostructures by a Facile Composite-Hydroxide-Mediated Route

Tauseef Shahid
Department of Applied Physics, Federal Urdu University of Arts, Science and Technology, Islamabad, Pakistan

Muhammad Arfan
Department of Applied Physics, Federal Urdu University of Arts, Science and Technology, Islamabad, Pakistan

Aurang Zeb
Department of Applied Physics, Federal Urdu University of Arts, Science and Technology, Islamabad, Pakistan

Tayyaba BiBi
FOCAS, Technological University Dublin (DIT), Dublin, Ireland

Taj Muhammad Khan
School of Physics, Trinity College Dublin (TCD), Dublin, Ireland

Follow this and additional works at: https://arrow.tudublin.ie/nanolart

Part of the Nanomedicine Commons

Recommended Citation

Preparation and physical properties of functional barium carbonate nanostructures by a facile composite-hydroxide-mediated route

Tauseef Shahid[1], Muhammad Arfan[1], Aurang Zeb[1], Tayyaba BiBi[2,3], and Taj Muhammad Khan[4,5]

Abstract

Recently, barium carbonate nanomaterial has been shown to be a proven versatile candidate for the catalysis and sensor applications. The catalytic and sensing efficiency can be improved by making barium carbonate composite with a suitable transition element. In this regard, the preparation of barium carbonate and its composite with nickel during the synthesis process is presented with the composite-hydroxide-mediated method, an effective, feasible, and low-temperature synthesis route. The nanomaterial produced is monitored for the structural and optical properties with various diagnostic methods. The X-ray diffraction results show the presence of orthorhombic structure of barium carbonate in both pure and 5% nickel samples. A mixed structure is formed with the phases of barium carbonate, $Ba(NO_3)_2$, and $Ni(NO_3)_2$ for the sample with 15% nickel. The average crystallite size estimated is in the range of 14–22 nm. The scanning electron microscope pictures captured on silicon (Si) covered with the product material reveal interesting rods, needle, and flower-type morphological features. The bandgap energy obtained by diffused reflectance spectroscopy is in the expected range of 5.48–5.71 eV. The proposed method seems effective to provide a feasible route for the synthesis of a broad range of nanomaterials for research purposes.

Introduction

In recent years, nanotechnology has given birth to numerous nanomaterials due to their increased use in various sectors of research and development. To produce these nanomaterials, nanotechnology further has opened several rooms for the potential novel methods. Composite-hydroxide-mediated (CHM) method is one of the recent chemical synthesis routes that have gained considerable importance in research due to their effortlessness and versatile nature, covering a broad range of nanomaterials to

[1] Department of Applied Physics, Federal Urdu University of Arts, Science and Technology, Islamabad, Pakistan
[2] Department of Chemistry, Peshawar University, Pakistan
[3] FOCAS, Dublin Institute of Technology (DIT), Dublin, Ireland
[4] National Institute of Lasers and Optronics (NILOP), Islamabad, Pakistan
[5] School of Physics, Trinity College Dublin (TCD), Dublin, Ireland

Corresponding author:
Taj Muhammad Khan, National Institute of Lasers and Optronics (NILOP), Islamabad 44000, Pakistan.
Email: tajakashne@gmail.com

prepare. Compared to other chemical methods, CHM is quite a simple and environmentally appealing method. CHM is a straightforward approach, based on the use of molten hydroxides (NaOH:KOH) and basic source material.[1] Recently, this method has been used to prepare a variety of nanostructures including $BaTiO_3$, CdO, ZnO, NiO, and so on.[2–5] Shahid et al. have applied this method to prepare Zn(II)-CuO composite and probed the structural and optical properties.[6] The reported results show that the method seems to be a feasible and an effective route to produce various composites directly during the synthesis process. In this work, we have considered this approach for the synthesis of barium carbonate ($BaCO_3$) and Ni-$BaCO_3$ composites.

In heavy metal carbonates, $BaCO_3$ is an important material with industrial applications.[7–18] It crystallizes into three polymorphisms (i.e. orthorhombic, hexagonal, and cubic), but only the orthorhombic phase is obtained under the ambient conditions. $BaCO_3$ is a thermodynamically stable crystal compared to other heavy metal carbonates (ACO_3, A = Sr, Pb, and Ba). Nano-$BaCO_3$ has several potential applications in diverse fields of science and technology.[7–18] Compared to other metal catalysts, $BaCO_3$ nanoparticles and their composite nanostructures have shown improved catalytic activity for the excellent performance of solid-oxide fuel cell cathodes through the enhanced kinetic surface reaction process.[13] High degree of electrochemical activity has been reported for the magnesium-doped $BaCO_3$ ($BaMn_{0.51}C_{0.49}O_3$) cathode material produced by hydrothermal process.[14] In a recent report, the controlled structures and luminescence properties of lanthanide-doped $BaCO_3$ through synthesis strategy have greatly facilitated the development of novel optical materials for photonic devices.[15] It is also a well-known precursor material for the magnetic ferrites and gas sensor application.[11,18] Even though nanosized $BaCO_3$ can be produced. by different techniques like sol-gel techniques, auto-combustion of citrate–nitrate gel, CHM, microemulsion-mediated solvothermal route, the reversed micelles method, the semi-batch crystallizer process, self-organized formation, microwave-assisted route, sonochemical synthesis, electro-deposition, CHM, and so on,[14–34] CHM methodology is an attractive route in many aspects to synthesize $BaCO_3$ nanomaterial in various morphologies and offers several other advantages. Technically, the method is sound, friendly to environment, and easy to apply for the preparation of a wide range of significant nanostructures. The present paper is closely relevant to the work previously done in the group.[2–6] The aim of the work is to further investigate potential of the method for a large production of various nanomaterials for research purposes.
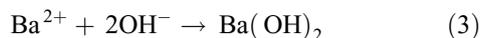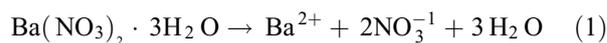
In this article, we have described the synthesis of pure and Ni-$BaCO_3$ nanostructured composites with the CHM approach and examined feasibility of the method for low and high nickel contents at various synthesis conditions. The prepared nonmaterial has been monitored using X-ray diffraction (XRD), Fourier-transform infrared spectroscopy (FTIR), diffused reflectance spectroscopy (DRS), and scanning electron microscopy (SEM). Influence of the incorporated nickel has been investigated on the structural, morphological, and optical properties, and formation mechanisms are explicated. The method seems quite fit for the synthesis of pure Ni-$BaCO_3$ composites and is expected to yield a wide range of technologically important composite nanomaterials for the sensing and catalysis applications.

Experimental

Synthesis procedure

Chemical reagents were purchased from Merck Co. (Pharmaceutical Company, Darmstadt, Germany) with quoted purity 99.99%, hence used without any further purification, which included $Ba(NO_3)_2 \cdot 3H_2O$, $Ni(NO_3)_2 \cdot 3H_2O$, NaOH, and KOH. Experimental procedure for the synthesis of nanomaterials using CHM is given in our previous reports.[2–6] Briefly, a 10 g of mixed hydroxides (NaOH:KOH = 51.5:48.5) was taken in a Teflon vessel and heated up to 200°C in a preheated furnace. When the hydroxides were totally molten, an amount of 2.5 g of $Ba(NO_3)_2 \cdot 3H_2O$ was added and the mixture was stirred until a uniform precursor was obtained. This procedure was also done for Ni-$BaCO_3$ nanostructures (composites) where $Ni(NO_3)_2 \cdot 3H_2O$ was added in the quantities as 5% and 15%. The whole procedure lasted for about 24 h. A certain amount of precursor was dissolved in various volumes of deionized water. After aging for several hours, the product was filtered and washed thoroughly by deionized water to remove residual hydroxides. The washed crystals were dried at 40°C for 24 h. For $BaCO_3$ formation, the possible mechanism may be suggested as follows: NaOH and KOH play the same role in the composite hydroxide melts. The simplified expressions for chemical reactions are written as

$$Ba(NO_3)_2 \cdot 3H_2O \rightarrow Ba^{2+} + 2NO_3^{-1} + 3H_2O \quad (1)$$

$$NaOH \rightarrow Na^{+1} + OH^- \quad (2)$$

$$Ba^{2+} + 2OH^- \rightarrow Ba(OH)_2 \quad (3)$$

$$Ba(OH_2) + CO_2 \rightarrow BaCO_3 \downarrow + H_2 \quad (4)$$

Reactions up to $Ba(OH)_2$ formation are happened in the composite hydroxide melts in the Teflon vessel at 200°C, while the last reaction is expected to occur after the product is removed from the vessel. The obtained $Ba(OH)_2$ reacts with CO_2 in the atmosphere to form $BaCO_3$ thoroughly during the subsequent washing and drying process. NaOH and KOH are high melting point melts, but CHM approach basically involves the chemical reactions in the eutectic hydroxides melts at a temperature of approximately
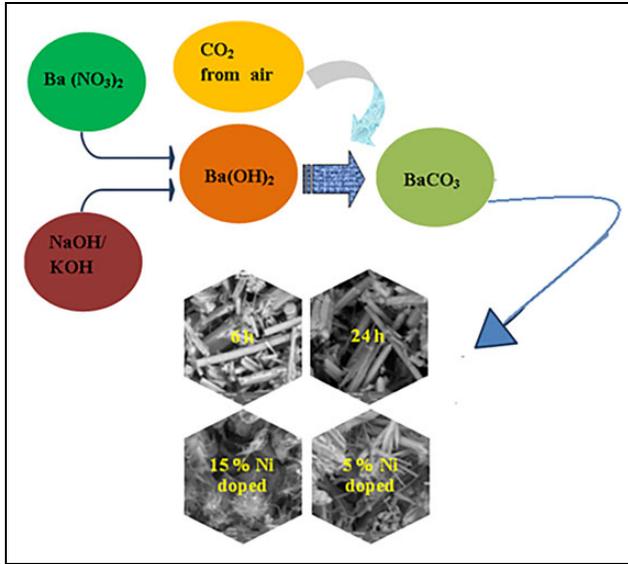
Figure 1. Sketch of the CHM method illustrating preparation of $BaCO_3$. CHM: composite-hydroxide-mediated; $BaCO_3$: barium carbonate.

200°C. These hydroxides are used as an important reaction medium to reduce the reaction temperature of the reactants for the preparation of a nanomaterial. A sketch of the procedure illustrating all the basic steps involved in the preparation of $BaCO_3$ from the basic salts is depicted in Figure 1.

Characterization methods

Various diagnostic methods were employed to examine the formation of nanomaterial. XRD was done using the PANalytical diffractometer Bruker D-8 Discover X-ray diffractometer equipped with a CuKα-radiation (λ = 1.54186 A). FTIR (Perkin Elmer NICOLET-6700) of Thermo Electron Corporation, spectral range between 400–4000 cm^{-1}. The samples were scanned for 2θ values in the range of 20–80° with a step size of 0.02°. Morphological analysis was made on the sample with electron microscopy using a BSE detector operated at 10 kV.

FTIR spectrum was studied with a PerkinElmer FTIR spectrometer in the required spectral range of 400–3000 cm^{-1} to probe the functional groups and the stretching vibration of C–O bond in $BaCO_3$. The DRS spectra of the samples were measured in the range of 200–1500 nm using a PerkinElmer Ultra-violet (UV)/ Visible (VIS)/Near infrared (NIR) Spectrometer Lambda 950 and the acquired data were used to estimate the optical bandgap.

Results and discussion

XRD is employed at the first instant to test and monitor the crystallized phases and impurity traces in the prepared material. These results are displayed in Figure 2(a) and

(b). For the pure and 5% samples, all the observed diffraction peaks at 2θ values correspond to the reflection planes of $BaCO_3$. The sharp diffraction peaks demonstrate the formation of a single-phase polycrystalline orthorhombic $BaCO_3$. In both samples, no diffraction peak was recorded for any impurity traces. The XRD pattern obtained is closely matched with the reference pattern of $BaCO_3$ (JCPDS# 00-005-0378). The peak intensities of (111) and (112) crystallographic planes shown in Figure 2(b) suggest that the orientation of most of the crystallites is along these planes. The 2θ reflection is lower angle shifted for the 5% nickel sample, which suggests incorporation of nickel impurity at the lattice sites. For the higher value nickel content of 15%, a departure from pure in to a mixed structure was observed, with the structure composed of the identified phases of $BaCO_3$, $Ba(NO_3)_2$, and $Ni(NO_3)_2$. The average crystallite sizes calculated are tabulated in Table 1. The value of average grain size (D) was estimated with the Debye–Schrrer formula[35]

$$D = \frac{K\lambda}{\beta \cos \theta} \qquad (5)$$

where λ is the wavelength of the Cu Kα line (in nm) used, K is the shape factor, θ is Bragg's angle, and β is the full width at half maximum.

The micro strain (ε) was calculated using the following relation called the Williamson–Hall method[36]

$$\varepsilon = \frac{\beta \cos \theta}{4} \qquad (6)$$

The dislocation density (δ)[37] and X-ray density[38] were also calculated using the formulas

$$\delta = \frac{1}{D^2} \qquad (7)$$

$$\rho_{X-ray} = \frac{ZM}{V_{cell}N_A} \qquad (8)$$

where "Z" is the number of molecules per formula unit, "M" is the molar mass, "N_A" is the Avogadro constant, and V_{cell} is the volume of unit cell. For dislocation density, the average grain size was used in equation (7). All the calculated structural parameters with average grain size are listed in Table 1. Clearly, the lattice parameters for the pure and 5% Ni-$BaCO_3$ composites are closely in the range with standard values already reported in the literature. A significant change is noticed for the sample with 15% nickel. An overall increase in the crystallite size is observed with nickel.

For the chemical signature on the final product, FTIR spectra of the samples are given in Figure 3. The samples show characteristics vibration peaks of CO_3^{-2} in the range of 400–1800 cm^{-1}. As evident from the figure, the strong absorption peaks observed at 694 and 854 cm^{-1} are assigned to the bending out-plane and in-plane vibrations of the (O–C–O) (CO_3^{-2}) bonds, respectively.[39] The absorption bands at 1060 cm^{-1} are related to the symmetric
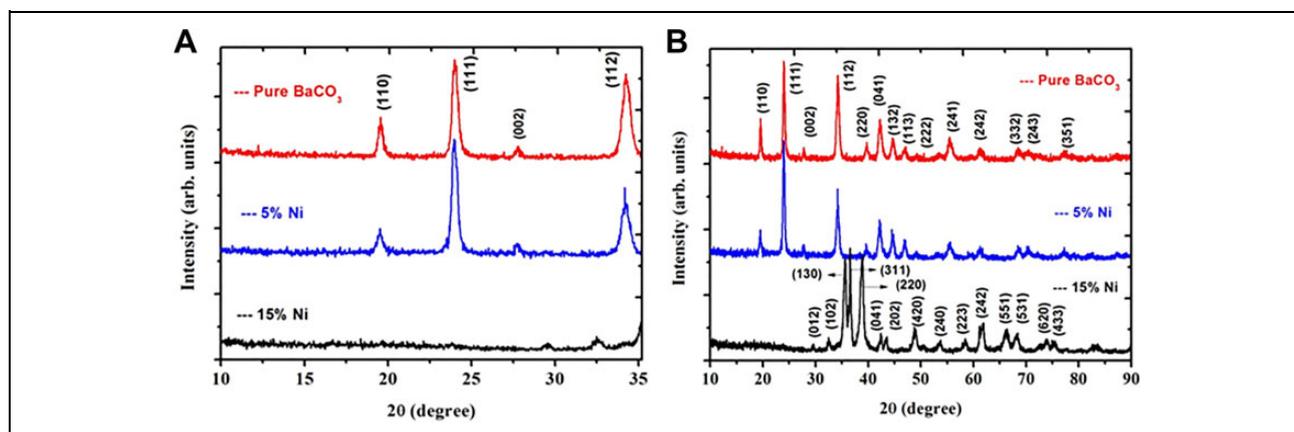
Figure 2. (a) XRD pattern of $BaCO_3$ nanomaterial prepared with CHM method for the pure, 5%, and 15% nickel samples (b) shows how preferential growth of the nanomaterial along particular planes depends on the low and high concentration of nickel. XRD: X-ray diffraction; CHM: composite-hydroxide-mediated; $BaCO_3$: barium carbonate.

Table 1. Structural parameters of pure and Ni-$BaCO_3$ composite nanomaterial calculated from the XRD measurements.

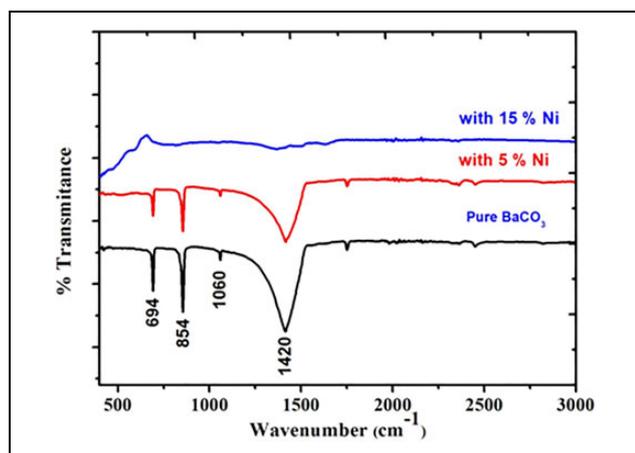| Nickel content (%)	Crystallite size (nm)	X-ray density (g cm^{-3})	a (Å)	b (Å)	c (Å)	Cell volume (Å^3)	Micro strain	dislocation density (m^{-1})
0 (pure)	14	4.3	0.525	9.04	6.40	304.54	0.00275	5×10^{15}
5	18	4.31	0.524	9.04	6.41	304.42	0.00232	3×10^{15}
15	22	4.29	0.532	8.84	6.47	305.01	0.00192	2×10^{15}

XRD: X-ray diffraction; $BaCO_3$: barium carbonate.

Figure 3. FTIR spectra of the pure and nickel-based composites (5% and 15%) of $BaCO_3$ nanostructures prepared at 200°C for a constant reaction time of 24 h. FTIR: Fourier transform infrared; $BaCO_3$: barium carbonate.

stretching mode of C–O bond, whereas the bands at 1420 cm^{-1} are attributed to an asymmetric stretching vibration of the C–O bond.[40]

With the aim to assess the microstructure and morphology of $BaCO_3$ and Ni-$BaCO_3$ composite nanomaterials, a detailed analysis of the samples was done using electron microscopy. The SEM micrographs with low and high magnification are illustrated in Figure 4(a) to (f). Interesting hexagonal, needle, rods, and peony flower–type dense nanostructures are formed. Clearly, morphology of the nanostructure seems to change with nickel and seems strongly to depend on the added content of nickel. The microstructures are connected together on the bases, rooted in one center, and presented a beautiful rod and flower-like morphologies. The pure $BaCO_3$ sample has rod-like orientation which is hexagonal-shaped as observed in the XRD results. From the SEM images, it seems that the rods are hollow, while the Ni-$BaCO_3$ composite prepared at the same condition presents needle-like rods and flower-like structure. An interesting morphological structure is formed as the concentration of nickel was increased to 15%, where a mixed-type structure is formed. It is noteworthy to mention here that clearly rod-type morphology is obtained when the reaction time was reduced by four times the initial processing time. For the shorter reaction time of 6 h (Figure 4(g) and (h)), material is nucleated in the form of rods with an average diameter in the range of 0.130 to 0.54 μm. This validates the time-dependent mechanisms of crystallization of a nanomaterial with the CHM method. The nucleation and subsequent formation mechanisms of $BaCO_3$ nanomaterial is based on the higher concentration of OH$^-$ ions in the growth solution and viscosity of the melts at the processing temperature. Both the hydroxide ions and viscosity of the melts favor to speed up formation process of $BaCO_3$ peony flower nanostructures due to larger number of growth nuclei sites. At the beginning, only a few $BaCO_3$ nuclei are produced; however, as the growth process
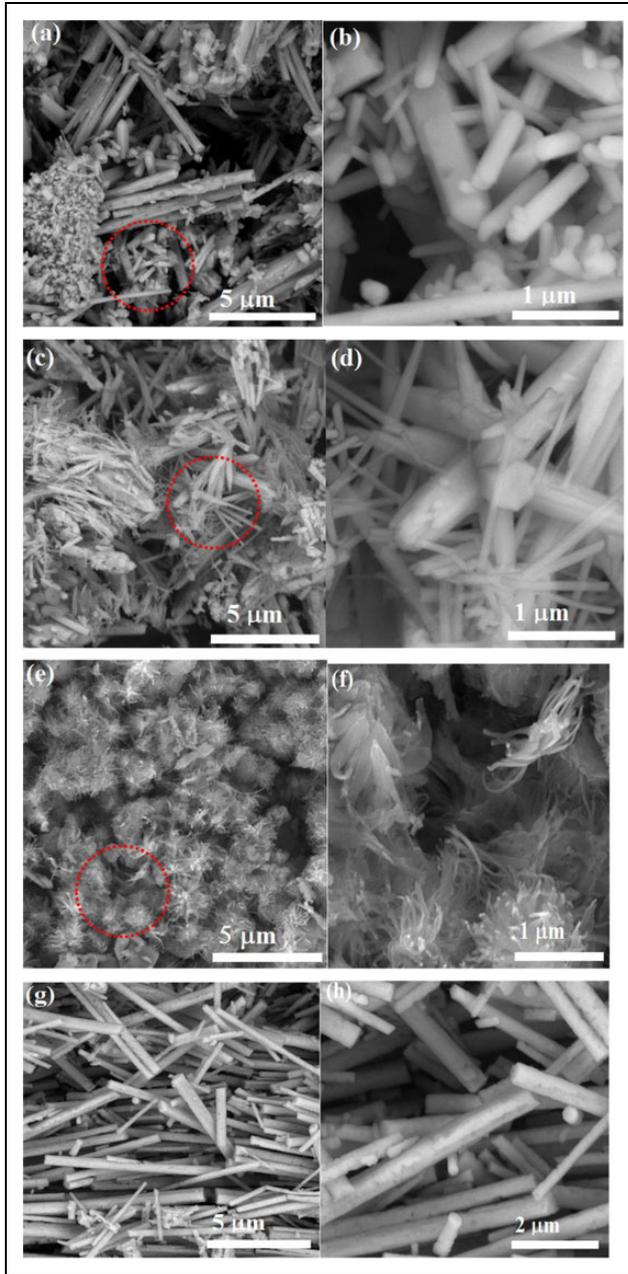
Figure 4. SEM images of $BaCO_3$ nanostructures captured at two different magnifications prepared by CHM at 200°C and processing time of 24 h. (a, b) Pure $BaCO_3$, (c, d) 5% nickel, (e, f) 15% nickel, and (g, h) $BaCO_3$ prepared at 200°C and reaction time of 6 h. SEM: scanning electron microscope; CHM: composite-hydroxide-mediated; $BaCO_3$: barium carbonate.

progresses, surfaces of the produced $BaCO_3$ nuclei either get a negative or a positive charge. The produced opposite charges (OH^- and Ba^{+2}) attract each other to form $Ba(OH)_2$, which further reacted with CO_2 to form $BaCO_3$ and hydrogen molecule. The effect of kinematic viscosity of the melts on the formation of $BaCO_3$ nanomaterial by CHM is still poorly understood due to the involved complex thermodynamics. However, it is noteworthy to

mention here that a high viscosity medium reduces the speed of nucleation, aggregation, and recrystallization and results in the formation of bigger crystallites in the final nanoproduct.

DRS was performed in order to investigate the optical behavior of the prepared $BaCO_3$ nanostructures. All the spectra were taken in the spectral range of 200–1500 nm. The DRS spectra variation of pure and composite Ni-$BaCO_3$ prepared for 24 h at a constant temperature and reaction time are shown in Figure 5(a). The Kubelka–Munk model is applied to find the optical bandgap of the prepared samples, while the direct bandgap energies can be estimated from a plot of $(F(R)h\nu)^2$ versus the photon energy ($h\nu$).[41] For this purpose, a well-known Kubelka–Munk function $F(R)^2$ was estimated by the formula[42]

$$F(R) = \frac{(1 - R)^2}{2R} \qquad (9)$$

and the bandgap energy was estimated by Tauc's equation[43]

$$F(R)\,h\nu = A(h\nu - E_g)^n \qquad (10)$$

where R is the reflectance, h is the plank's constant, ν is the frequency of the photon, $h\nu$ is the photon energy in eV, E_g is the optical band gap in eV, A is a constant, and n is an exponent which is 2 for indirect band transitions and 1/2 for direct band transition. The direct band gap energy for the samples can be estimated by extrapolating the linear region of $(F(R)h\nu)^2$ versus $h\nu$ to the point $F(R)^2 = 0$. Thus, the E_g is the intercept of the line at $h\nu$-axis. The obtained direct bandgap values are 5.51, 5.48, and 5.71 eV for the pure and 5% and 15% samples, respectively. The variation in bandgap of $BaCO_3$ with nickel is constant and shown in Figure 5(b). The value of bandgap first drops followed up by an increase with nickel. No significant change was found by the optical study in the behavior of electronic insulation characteristics of $BaCO_3$. A similar bandgap behavior was observed in previous study of NiO.[4] With grain size, the calculated bandgap shows quite a different behavior; initially it decreases and then increases and can be explained in two different frameworks. For the first case, we assume the decrease is due to the decrease in micro strain which reduces the strain energy and subsequently the bandgap energy drops. The internal micro strain strongly depends on the morphology which is different in our case and could be assuming coherent in our case of different morphological structures. For the second case, the crystallite size and energy bandgap (blueshift) are co-related by using the effective mass approximation. Under this approximation, the size dependence of the bandgap (E_{nano}) can be represented as follows[44]

$$E_{nano} = E_{bulk} + \left. \pi^2 h^2 \middle/ 8R^2 \left(1 \middle/ m_e^* + 1 \middle/ m_h^* \right) \right. - 1.8\,e^2 \middle/ 4\pi \varepsilon_0 \varepsilon_\alpha R$$
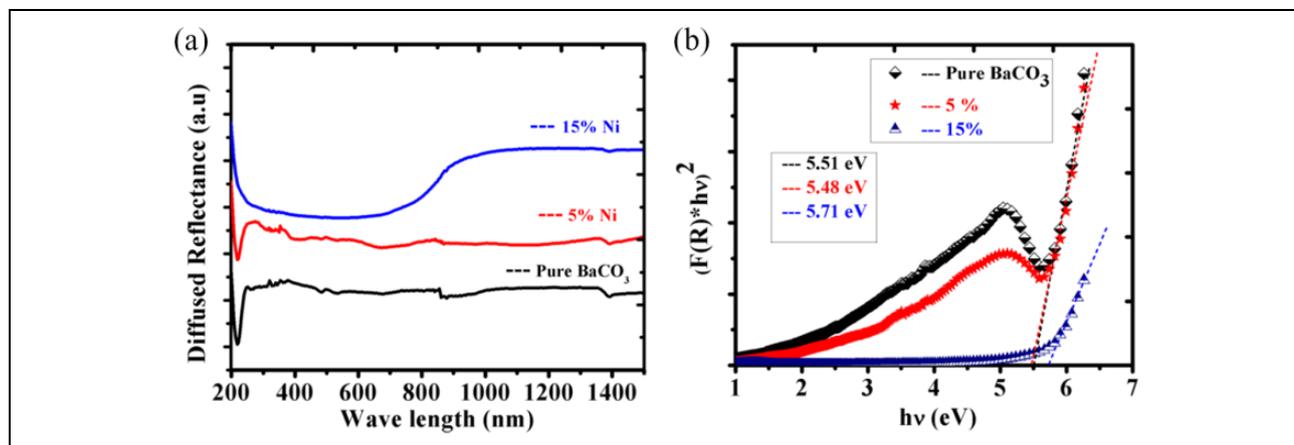
$$(11)$$

Figure 5. (a) Diffused reflectance spectra of the CHM prepared pure and nickel-based composite of $BaCO_3$ nanomaterial at 200°C and constant reaction time of 24 h. (b) The $(F(R) \, h\nu)^2$ versus $h\nu$ plot of as prepared pure $BaCO_3$ and Ni-$BaCO_3$ composite materials. E_g is the intercept of the line at $h\nu$-axis for the bandgap calculation. CHM: composite-hydroxide-mediated; $BaCO_3$: barium carbonate.

where E_{nano} and E_{bulk} are the bandgap of nano and bulk materials, respectively, m_e^* and m_h^* are the effective masses of electron and hole, respectively, ε_0 is the permittivity of the material, and ε_α is the high-frequency dielectric constant. Equation (11) is a clear manifestation of the energy bandgap showing R^{-2} dependence in the first term and R^{-1} dependence in the second term. Consistent to this dependence, as the grain size increases, the bandgap jumps from 5.51 to 5.71 eV accordingly. However, our value for the 5% sample shows a departure from this dependence and drops from 5.51 to 5.48 eV, and this behavior is quite consistent with our previous observation reported.[4] It is noteworthy to mention here that overall the bandgap values are quite close to each other to account for any significant change.

Conclusion

In summary, polycrystalline pure and Ni-$BaCO_3$ nanomaterial composites were prepared with the CHM method and examined for the structural and optical properties using various diagnostic methods. The average crystallite size was in the range of 14–22 nm and increased with nickel concentration. For the lower value of nickel, nanomaterial was crystallized in a single orthorhombic phase with no impurity traces. For 15% nickel content, a mixed structure was formed and showed the solubility and reaction limit of the source materials with CHM at a particular reaction temperature and processing time. The hexagonal rods, needle-type, and flower-like structures were observed in the SEM micrographs and were strongly dependent on the nickel content and reaction time. The estimated bandgap was in the range of 5.48–5.71 eV and suggested that the electronic insulation behavior of $BaCO_3$ was not changed considerably. These results manifest that CHM method is effective for the preparation of composite $BaCO_3$ and can be tested for synthesis of other nanocomposites.

References

1. Hu C, Xi Y, Liu H, et al. Composite-hydroxide-mediated approach as a general methodology for synthesizing nanostructures. *J Mater Chem* 2009; 19(7): 858–869.
2. Khan TM, Zakria M, Shakoor RI, et al. Composite-hydroxide-mediated approach an effective synthesis route for $BaTiO_3$ functional nanomaterials. *J Appl Phys A* 2016; 122: 274.
3. Khan TM, Shahid T, Zakria M, et al. Optoelectronic properties and temperature dependent mechanisms of composite-hydroxide-mediated approach for the synthesis of CdO nanomaterials. *Electron Mater Lett* 2015; 11(3): 366–373.
4. Shahid T, Khan TM, Zakria M, et al. Synthesis of pyramid-shaped NiO nanostructures using low-temperature composite-hydroxide-mediated approach. *J Mater Sci and Eng* 2016; 5(6): 6.
5. Khan TM, Zakria M, Shakoor RI, et al. Mechanisms of composite-hydroxide-mediated approach for the synthesis of functional ZnO nanostructures and morphological dependent optical emissions. *Adv Mater Lett* 2015; 6(7): 592–599.

6. Shahid T, Arfan M, Ahmad W, et al. Synthesis and doping feasibility of composite-hydroxide-mediated approach for the $Cu_{1-x}Zn_xO$ nanomaterials. *Adv Mater Lett* 2016; 7(7): 561–566.

7. Zhang H, Hu C, Zhang M, et al. Synthesis of $BaCO_3$ nanowires and their humidity sensitive property. *J Nanosci Nanotechnol* 2011; 11(12): 10706–10709.

8. Gutmann B and Chalup A. Barium carbonate. *Am Ceram Soc Bull* 1993; 72(6): 83–84.

9. Chen L, Shen Y, Xie A, et al. Nanosized barium carbonate particles stabilized by cetyltrimethylammonium bromide at the water/hexamethylene interface. *Cryst Res Technol* 2007; 42(9): 886–889.

10. Li J, Wei D, Hu Y, et al. Synthesis of ultrafine green-emitting $BaCO_3$ nanowires with 18.5 nm-diameter by CO_2 vapor-assisted electrospinning. *Cryst Eng Comm* 2014; 16(6): 964–968.

11. Macketta JJ. *Encyclopedia of chemical processing and design*, vol. 51. New York: Marcel Dekker, 1977.

12. Wenjie Z, Chunhua C and Jiaping L. Polymer micelle-directed growth of $BaCO_3$ spiral nanobelts. *Chem Commun* 2012; 48(68): 8544–8546.

13. Tao H, Kyle SB and Changrong X. Barium carbonate nanoparticles as synergistic catalysts for the oxygen reduction reaction on $La_{0.6}Sr_{0.4}Co_{0.2}Fe_{0.8}O_{3-x}$ solid-oxide fuel cell cathodes. *Chem Electro Chem* 2016; 3(5): 805–813.

14. Benjamin H, Lev S, Eric AS, et al. A manganese-doped barium carbonate cathode for alkaline batteries. *J Electrochem Soci* 2014; 161(6): A835–A840.

15. Jianmin G, Zhenpan B, Baipeng Y, et al. Simultaneous structure and luminescence property control of bariumcarbonate nanocrystals through small amount of lanthanide doping. *Sci Bull* 2017; 62(18): 1239–1244.

16. Wang LN, Huo JC, Liu SX, et al. A new route to the synthesis of barium carbonate crystals by the induction of *Bacillus pasteurii*. *Chinese J Struc Chem* (2011); 30: 738–742.

17. Zhang HY, Hong JM, Ni YH, et al. Microwave-assisted synthesis of $BaCO_3$ crystals with higher-order superstructures in the presence of SDS. *Cryst Eng Comm* 2008; 10: 1031–1036.

18. Kim DY, Hyuntae K, Choi N-J, et al. A carbon dioxide gas sensor based on cobalt oxide containing barium carbonate. *Sens Actuators B Chem* 2017; 248: 987–992.

19. Peng E, Wei X, Herng TS, et al. Ferrite-based soft and hard magnetic structures by extrusion free-forming. *RSC Adv* 2017; 7(43): 27128–27138.

20. Sreedhar B, Vani CS, Devi DK, et al. Nanosized barium carbonate particles stabilized by cetyltrimethylammonium bromide at the water/hexamethylene interface. *Am J Mater Sci* 2012; 2(4): 105–109.

21. Patnaik P. *Handbook of inorganic chemicals*, 1st ed. New York: McGraw-Hill, 2003, p. 529.

22. Tai C and Liu H. Synthesis of submicron barium carbonate using a high-gravity technique. *Chem Engin Sci* 2006; 61(22): 7479–7486.

23. Kandori K, Kon-no K and Kitahara A. Preparation of $BaCO_3$ particles in ionic w/o microemulsions. *J Disp Sci Technol* 1988; 9(1): 61–73.

24. Dewri R and Chakraborti N. Simulating recrystallization through cellular automata and genetic algorithms. *Modell Simula Mater Sci Eng* 2004; 13(2): 173–183.

25. Lv S, Sheng J, Zhang S, et al. Effects of reaction time and citric acid contents on the morphologies of $BaCO_3$ via PVP-assisted method. *Mater Res Bull* 2008; 43(5): 1099–1105.

26. Huang F, Shen Y, Xie A, et al. Polymorph control of a complex $BaCO_3$ superstructure through the cooperation of an insoluble polylactide self-assembled film and soluble poly allylamine modifier. *React Funct Polym* 2009; 69(11): 843–850.

27. Xu J and Xue D. Chemical synthesis of $BaCO_3$ with a hexagonal pencil-like morphology. *J Phys Chem Solids* 2006; 67(7): 1427–1431.

28. Nagajyothi PC, Muthuraman P, Sreekanth TVM, et al. In vitro anticancer potential of BaCO3 nanoparticles synthesized via green route. *J Photochem Photobiol* 2016; 156: 29–34.

29. Li L, Chu Y, Liu Y, et al. Microemulsion-based synthesis of $BaCO_3$ nano belts and nanorods. *Mater Lett* 2006; 60(17–18): 2138–2142.

30. Karagiozov C and Momchilova D. Synthesis of nano-sized particles from metal carbonates by the method of reversed mycelles. *Chem Eng Process Process Intensif* 2005; 44(1): 115–119.

31. Wang T, Xu A, and Cölfen H. Formation of self-organized dynamic structure patterns of barium carbonate crystals in polymer-controlled crystallization. *Angew Chem Int Ed* 2006; 45(27): 4451–4455.

32. Ma M-G, Zhu Y, Zhu J, et al. Microwave-assisted fabrication and characterization of $BaCO_3$ nanorods. *Chem Lett* 2006; 35(10): 1138–1139.

33. Dinamani M, Kamath PV and Seshadri R. Electrodeposition of $BaCO_3$ coatings on stainless steel substrates. *Cryst Grow Desig* 2003; 3(3): 417–423.

34. Alavi MA and Morsali A. Syntheses of $BaCO_3$ nanostructures by ultrasonic method. *Ultrason Sonochem* 2008; 15(5): 833–838.

35. Klug HP and Alexander LE. *Diffraction procedures for polycrystalline and amorphous materials*, 1st ed. New York: Wiley, 1954.

36. Gülen Y, Sahin B, Bayansal F, et al. Solution-phase synthesis of un-doped and Pb doped CdO films. *Superlattices Microstruct* 2014; 68: 48–55.

37. Javid MA, Rafi M, Ali I, et al. Synthesis and study of structural properties of Sn doped ZnO nanoparticles. *Mater Sci Pol* 2016; 34(4): 741–746.

38. Mushtaq S, Ismail B, Aurang Zeb M, et al. Low-temperature synthesis and characterization of Sn-doped Sb_2S_3 thin film for solar cell applications. *J Alloys Compd* 2015; 632: 723–728.

39. Alavi MA and Morsali A. Syntheses and characterization of Sr (OH)$_2$ and SrCO$_3$ nanostructures by ultrasonic method. *Ultrason Sonochem* 2010; 17(1): 132–138.

40. Sreedhar B, Satya Vani C, Keerthi Devi D, et al. Biomimetic mineralization of BaCO$_3$ microstructures by simple CO$_2$ diffusion method. *Am J Mater Sci* 2012; 2(4): 105–109.

41. Khorsand Zak A, Yousefi R, Majid MA, et al. Facile synthesis and X-ray peak broadening studies of Zn$_{1-x}$ Mg$_x$ O nanoparticles. *Ceram Int* 2012; 38(3): 2059–2064.

42. Wang D, Zhao S, Xu Z, et al. The improvement of near-ultraviolet electroluminescence of ZnO nanorods/ MEH-PPV heterostructure by using a ZnS buffer layer. *Org Electron* 2011; 12(1): 92–97.

43. Jan T. *Optical properties of amorphous semiconductors, in amorphous and liquid semiconductors*. USA: Springer, 1974, pp. 159–220.

44. Khan TM and Hussain B. Study of UV-green emissions and spectroscopic properties of polycrystalline ZnO thin films. *Int J of Chem Mate Sci* 2015; 3(1): 001–011.